Self-consistent, one-dimensional analysis of the Hall effect thruster

2011 Plasma Sources Sci. Technol. 20 045021

(http://iopscience.iop.org/0963-0252/20/4/045021)

Plasma Sources Sci. Technol. **20** (2011) 045021 (15pp) doi:10.1088/0963-0252/20/4/045021

Self-consistent, one-dimensional analysis of the Hall effect thruster

Kybeom Kwon[1], **Mitchell L R Walker**[2] **and Dimitri N Mavris**[2]

[1] Department of Aerospace and Mechanical Engineering, Republic of Korea Air Force Academy, Chungbuk 363-849, Republic of Korea
[2] Department of Aerospace Engineering, Georgia Institute of Technology, Atlanta, GA 30332, USA

E-mail: kybeom_kwon@gatech.edu

Received 18 October 2010, in final form 17 May 2011
Published 7 July 2011
Online at stacks.iop.org/PSST/20/045021

Abstract
This work achieves a self-consistent, robust, one-dimensional, macroscopic numerical model of the Hall effect thruster (HET) by dividing the discharge into two domains: (1) a collisionless electron diffusion region and (2) a collisional dominant electron diffusion region. Each region is modeled by governing equations based on the dominant physical characteristics. The solution for the discharge channel is created by matching the regional solutions at a common interface. The point validation for the model shows that the predicted HET performance is within 8% of the measured value. Furthermore, the proposed analysis is quite efficient in terms of a numerical perspective with a conventional PC wall time of 22 s for the nominal operating condition of the SPT-100. In addition, this paper shows that the numerical experiments for anomalous coefficients provide sufficient accuracy for performance metrics, closely matching the experimental data with correct values of the anomalous coefficients over a wide range of anode mass flow rates.

Nomenclature

A	thruster channel area
B	magnetic field strength
E	electric field strength
e	electrical charge
g_0	gravitational acceleration at the Earth's surface
K	magnetic field shape coefficient
k	Boltzmann constant
I_d	discharge current
I_{sp}	specific impulse
$I_{sp,ano}$	anode specific impulse
$I_{sp,tot}$	total specific impulse
$L_{presheath}$	presheath region length
m_e	electron mass
m_i	ion mass
m_n	neutral mass
$\dot{m}$	propellant mass flow rate
$\dot{m}_a$	anode mass flow rate
$\dot{m}_{n,c}$	neutral mass flow rate at the cathode
$\dot{m}_{i,c}$	ion mass flow rate at the cathode
n_e	plasma number density
$n_{e,m}$	plasma number density at the matching point
n_n	neutral number density
P_{cath}	power required to operate the cathode
P_d	discharge power
P_{mag}	power required to produce the magnetic field
P_{tot}	total power
RR	reaction rate
S	ionization source term
T	thrust
T_e	electron temperature
$T_{e,m}$	electron temperature at the matching point
t	time variable
u_e	electron mean velocity
u_i	ion mean velocity
$u_{i,c}$	ion mean velocity at the cathode line
$u_{i,0}$	ion mean velocity at the matching point
u_n	neutral mean velocity
$u_{n,c}$	neutral mean velocity at the cathode
$u_{n,0}$	neutral mean velocity at the matching point
V	dependent variable vector
V_d	discharge voltage
v_e	electron velocity
z	thruster axial coordinate
α_{ano}	anomalous electron diffusion coefficient

$\hat{\alpha}_{ano}$	inverse of the anomalous electron diffusion coefficient
α_{relax}	relaxation coefficient
ε_e	electron internal energy
ε_{exc}	threshold energy of first excitation level for xenon
ε_{ion}	threshold energy of first ionization for xenon
ε_0	permittivity of free space
Γ_e	electron flux
Γ_i	ion flux
Γ_n	neutral flux
η	efficiency
η_{ano}	anode efficiency
η_{tot}	total efficiency
φ	electric potential
φ_{edge}	electric potential at the Tonks–Langmuir edge
φ_d	discharge voltage
φ_m	electric potential at the matching point
μ	electron cross field mobility
ν_{ei}	Coulomb collision frequency
ν_{en}	electron–neutral momentum collision frequency
ν_{exc}	excitation collision frequency
$\nu_{e,eff}$	effective electron momentum collision frequency
$\nu_{e,m}$	classical cross field electron momentum collision frequency
$\nu_{e,\varepsilon}$	electron energy loss frequency
ν_i	ionization collision frequency
$\nu_{i,ave}$	average ionization collision frequency in the presheath region
ν_{recom}	recombination collision frequency
ν_{wall}	electron–wall collision frequency
σ	surface charge density
σ_i	ionization collision cross section
ω_e	electron cyclotron frequency
$\ln \Lambda$	Coulomb logarithm

1. Introduction

The space application demands on the Hall effect thruster (HET) as a plasma propulsion device continue to increase [1]. In the past 20 years, the numerical analysis for this specific device has steadily evolved. There have been three major categories of numerical analyses of the Hall thrusters: kinetic, fluid, and hybrid methods. Kinetic modeling attempts to solve the Boltzmann equation numerically. Because a correct mathematical representation of the time variation of the particle distribution function by collisions is not available for most physical situations, kinetic modeling often uses the collision probability concept in order to capture collisional effects on the distribution function. Several researchers have attempted a full kinetic modeling approach to simulate the HET [2–5]. The main advantage of this approach is that it can provide information about detailed physics such as the electron energy distribution function, sheath characteristics, and even startup transients. A drawback is computational inefficiency even in current high computer capability environments. In the fluid approach, the plasma properties of interest are macroscopic, not the details from microscopic views. Correct mathematical interpretations for fluid description are obtained by taking the moments of the Boltzmann equation in the velocity space. The terms that include the time variation of the particle distribution function caused by collisions should be converted into terms expressed by macroscopic variables. Although the fluid approach is computationally efficient, it cannot resolve the aforementioned detailed physics on a macroscopic scale. Various researchers have attempted the fluid approach to investigate macroscopic behaviors of the HET [6–13]. Quasi-neutrality is often assumed. The simplest approach using this method is to take the steady-state form of the governing equations and construct a system of ordinary differential equations (ODEs) for dependent variables. In this case, an internal regular singular point and an irregular singular point at the anode edge must be carefully dealt with. In addition, the initial guesses must often be close to the actual value. This reduces the robustness of the numerical method. Because of these numerical difficulties, some researchers neglect the anode sheath and assign arbitrary boundary values at the anode sheath edge, which can potentially degrade the self-consistency of the method [6–8, 10–13]. Self-consistency of concern is defined such that once a specific model is chosen, all of the unknown variables must be determined by this model. There should be no unknowns that must be set to arbitrary values. Another recent fluid model is solved using the time-explicit upwind scheme and the Harten–Lax–van Leer scheme for a conservative hyperbolic system with a rather complicated solution procedure [14]. The hybrid method combines kinetic and fluid modeling approaches. Typically, electrons are modeled as a fluid, while neutrals and ions are treated as particles. Several researchers have used this approach to simulate the HET [15–18]. Since the constraints on time step and grid spacing often come from electron analysis in the kinetic method, if the electrons are treated as a fluid, these constraints can be considerably diminished. However, in spite of these advantages, the hybrid method still suffers from computational inefficiency due to the inherent multiple time scale problems of the HET. In particular, the converged solutions for electron properties must be obtained at every ion/neutral time step.

In spite of the state of the art of numerical analysis of the HET, its design largely depends on expensive, time-consuming experiments [19]. Because the typical design process starts with a large design space, the numerical analysis in this step should have characteristics of numerical efficiency, self-consistency and robustness while providing a capability of representing sufficiently the physics involved.

In this paper, a self-consistent, robust and efficient one-dimensional (1D) macroscopic fluid model is presented for the purpose of implementing it into the conceptual design of new HETs. The model is quantitatively validated with experimental data at the design operation point of the SPT-100 incorporating the anomalous coefficient variation.

2. Model concepts

Due to the high computational cost of the kinetic and hybrid methods, a 1D macroscopic fluid model with sufficient

physical representation is considered. The governing equations are obtained by taking the moments of the Boltzmann equation and are solved with a time marching scheme. However, due to inherent multiple time scale characteristics of the current problem, the steady-state form of governing equations is used for numerical efficiency. In order to eliminate the need to solve Poisson's equation, quasi-neutrality is assumed as adopted in most of the previous 1D fluid models.

Many previous models that employ a fluid description suffer from a loss of self-consistency because of the arbitrary boundary values used at the edge of the anode sheath. An inconsistent solution should not be used for the approximation of actual thruster performance or behavior. In order to achieve self-consistency, the physics near the anode region must be properly modeled. It should be noted that there are two different phenomena possible for the anode sheath in a HET plasma; positive and negative anode falls [20]. The positive anode fall is electron attracting while the negative anode fall is electron repelling. The type of anode fall is dependent on anode cleanliness, discharge voltage and other operational parameters [20–22]. However, several experiments have confirmed the existence of negative anode fall [23–25]. Furthermore, several numerical methods successfully solve the HET operational characteristics with the negative anode fall boundary condition [26, 27]. The positive anode fall can result in discharge extinguishment in low propellant mass flow rate operation [26]. Thus, the negative anode fall is taken as one of the general physical phenomena in the HET. It can also be confidently applied to a new HET by designing it with a sufficiently low magnetic field near the anode region. For the case of negative anode fall, the ion backflow must meet the Bohm criterion at the Tonks–Langmuir edge [28].

Ahedo *et al* use a self-consistent 1D macroscopic fluid model that includes the boundary condition at the anode sheath and the ion backflow phenomenon [29, 30]. They use the shooting method for the resultant two-point boundary value problem (TPBVP). In order to avoid the difficulty in treatment of singular points and eliminate the initial guess dependence, the following strategy of solving a system of ODEs is used. Each ODE, before making the singular formulation for a selected dependent variable, is solved sequentially while other variables remain constant. Then each ODE is iteratively solved to obtain the convergent solution. Under-relaxation strategy can also be applied to enhance numerical robustness. However, there is still a numerical singularity problem when the ion momentum equation is solved. Equation (1) shows the ion momentum equation:

$$\frac{\mathrm{d}(m_\mathrm{i} n_\mathrm{e} u_\mathrm{i}^2)}{\mathrm{d}z} + n_\mathrm{e}\frac{\mathrm{d}(e\varphi)}{\mathrm{d}z} = m_\mathrm{i} n_\mathrm{e}(\nu_\mathrm{i} - \nu_\mathrm{recom})u_\mathrm{n} \tag{1}$$

where m_i is the ion mass, n_e is the plasma number density, u_i is the ion mean velocity, e is the electrical charge, φ is the electric potential, ν_i is the ionization collision frequency, ν_recom is the recombination collision frequency, u_n is the neutral mean velocity and z is the thruster axial coordinate. Equation (1) is solved for the ion mean velocity while the electric field $-(\mathrm{d}(e\varphi)/\mathrm{d}z) = eE$ and other variables may be fixed as constants. The resultant equation is written as

$$\frac{\mathrm{d}u_\mathrm{i}}{\mathrm{d}z} = \frac{n_\mathrm{e}}{m_\mathrm{i}\Gamma_\mathrm{i}} eE + \frac{n_\mathrm{e}(\nu_\mathrm{i} - \nu_\mathrm{recom})(u_\mathrm{n} - u_\mathrm{i})}{\Gamma_\mathrm{i}} \tag{2}$$

where Γ_i is the ion flux. The ion flux term sits in the denominators of the right-hand side of equation (2). If the physics of ion backflow are included, it is definitely expected that the ion flux term has a range of values from negative at the anode to positive at the cathode, which means there is a point where the ion flux must be zero. This also causes another kind of regular singular point. Thus, another singularity causes the same difficulty. Note that at this regular singular point, the electric field must approach zero. In addition the neutral and ion mean velocities must approach the same value.

In order to avoid this difficulty, the physics of electron phenomena in the HET is considered. In the exhaust region where the strength of the radial magnetic field is usually high, the electrons are magnetized by the strong radial magnetic field. In the region near the anode where the strength of the radial magnetic field is almost negligible, the electrons almost purely diffuse directly toward the anode. From this observation, we may assume that the solution domain may be divided into two regions in terms of electron dynamics: a collisional diffusion dominant region and a pure collisionless diffusion dominant region. The common interface linking these two regions should be the point where the ion mean velocity is equal to zero. The upstream region of the matching point will contain sheath and presheath regions and the downstream region will contain ionization and acceleration regions. These two regions are mathematically distinguished mainly by the treatment of the electron momentum equation. The electron momentum equation, with the assumptions of steady state, negligible electron inertia terms, stress tensor reduced to pure pressure, with a much higher electron velocity than those of other species, and azimuthal electron velocity obtained from stochastic analysis of the Langevin equation, is given by

$$0 = -\frac{\mathrm{d}(n_\mathrm{e} k T_\mathrm{e})}{\mathrm{d}z} + n_\mathrm{e}\frac{\mathrm{d}(e\varphi)}{\mathrm{d}z} - m_\mathrm{e} n_\mathrm{e} \nu_\mathrm{e,eff}\left(1 + \frac{\omega_\mathrm{e}^2}{\nu_\mathrm{e,eff}^2}\right) u_\mathrm{e} \tag{3}$$

where k is the Boltzmann constant, $\nu_\mathrm{e,eff}$ is the effective electron momentum collision frequency, ω_e is the electron cyclotron frequency and u_e is the electron mean velocity. Equation (3) is reduced to the different forms for each divided region given below:

Collisionless pure diffusion region (upstream region)

$$0 = -\frac{\mathrm{d}(n_\mathrm{e} k T_\mathrm{e})}{\mathrm{d}z} + n_\mathrm{e}\frac{\mathrm{d}(e\varphi)}{dz}. \tag{4}$$

Collisional diffusion dominant region (downstream region)

$$0 = n_\mathrm{e}\frac{\mathrm{d}(e\varphi)}{\mathrm{d}z} - m_\mathrm{e} n_\mathrm{e} \nu_\mathrm{e,eff}\left(1 + \frac{\omega_\mathrm{e}^2}{\nu_\mathrm{e,eff}^2}\right) u_\mathrm{e}. \tag{5}$$

The two regions are solved independently via (4) and (5) and the properties at the common interface must match for all dependent variables. Note that the location of the common interface must also be solved. This treatment ensures both numerical robustness and self-consistency as shown in the following sections.

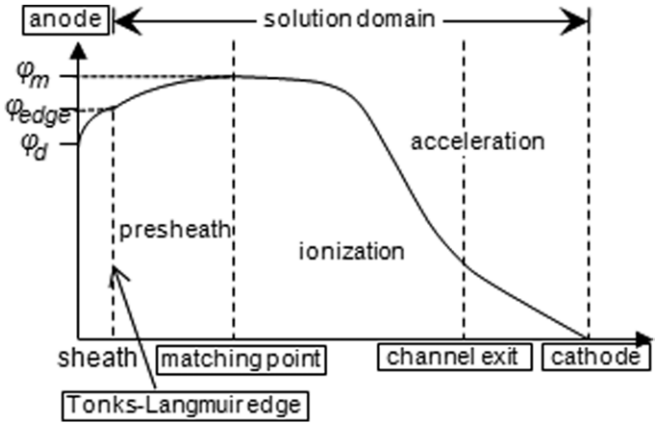

Figure 1. Expected solution structure for electric potential.

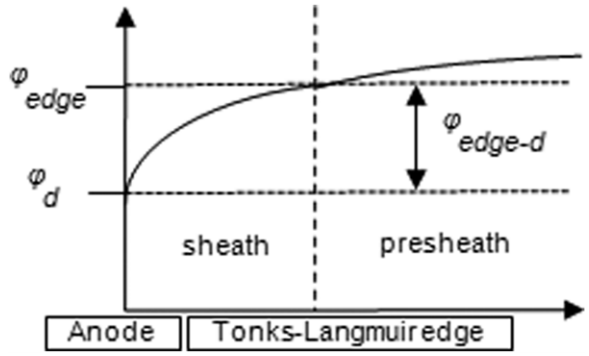

Figure 2. Schematic of electric potential distribution in the anode sheath region.

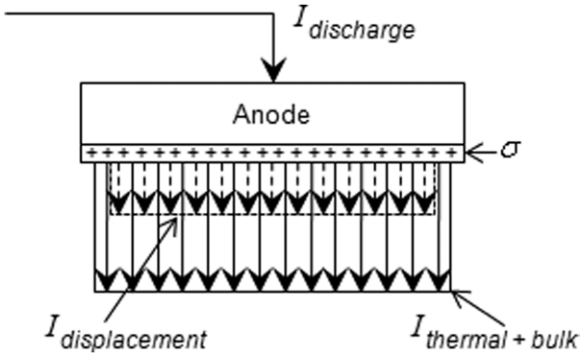

Figure 3. Currents and surface charge at the anode.

3. Model formulation

The analysis domain extends from the anode line to the cathode line. The region from the anode line to the Tonks–Langmuir edge is analyzed only for potential difference.

Since the negative anode fall is taken as a general plasma behavior near the anode region, the electric potential distribution is expected to be similar to the one as shown in figure 1, where φ_d is the electric potential at the anode which is the same as the discharge voltage, φ_{edge} is the electric potential at the Tonks–Langmuir edge and φ_m is the electric potential at the matching point. The solution domain is divided into two regions: the presheath region and the ionization/acceleration region.

Most assumptions made are taken from previous work using a 1D macroscopic model such as steady state, azimuthal symmetry, quasi-neutrality and constant neutral mean velocity based on assumed anode temperature at 1000 K. Further, neutral and ion temperatures are neglected. The electron stress tensor is reduced simply to isotropic pressure. The velocity distribution function of electrons is assumed to be Maxwellian. Neutrals and ions are assumed to be collisionless and radiative collisions are neglected.

The specific assumptions made here are that ion plume expansion is not considered so that the cross-sectional area of the channel is assumed to be constant throughout the domain. Only singly-charged ions are considered. In addition, the electron temperature in the sheath/presheath region is assumed to be constant since the presheath region is assumed to be collisionless except for the electron–neutral ionization collisions. Azimuthal drift electron kinetic energy is neglected compared with electron internal energy, and electron heat conduction, which has a tendency of smoothing the electron temperature profile [9], is neglected. Finally, ion recombination at the dielectric wall is not considered.

3.1. Anode sheath region

In this region, the information on $\varphi_{edge\text{-}d} = \varphi_{edge} - \varphi_d$ is only required as shown in figure 2.

The current balance relation at the anode is obtained by observing figure 3.

The currents involved are discharge current $I_{discharge}$, displacement current $I_{displacement} \propto dE/dt$ and the currents from the plasma by thermal flux and bulk movements of charged particles $I_{thermal+bulk}$. σ is the surface charge density at the anode. The current balance relation is simply current continuity around the anode, which is given by

$$I_{discharge} = I_{thermal+bulk} + I_{displacement}. \tag{6}$$

When the discharge current is smaller than the thermal and bulk currents from the plasma, the displacement current must be negative and the negative surface charge density is formed [31]. Since most currents are carried by electrons at the Tonks–Langmuir edge [20], the relative potential of plasma body to the anode potential at steady state when the displacement current vanishes is given by [32]

$$e\varphi = -kT_e \ln \frac{I_{discharge}}{I_{thermal+bulk}}. \tag{7}$$

Because the bulk electron mean velocity should be of the same order of magnitude as the thermal velocity in order to have a discharge current [20], the plasma current from the thermal flux and bulk movement of electrons would be almost twice that of the discharge current. Therefore, equation (7) is reduced to the following relation:

$$e\varphi_{edge\text{-}d} = kT_e \ln 0.5 \approx 0.6931 kT_e. \tag{8}$$

This approximation of the electric potential difference in the sheath is quite simple. However, the order of magnitude of the

electric potential difference should be the one given in (8) and it is acceptable in view of the current purpose.

It is noted that the potential difference between the anode and the Tonks–Langmuir edge is only a function of electron temperature in this approximation. Since the electron temperature in the sheath/presheath region is assumed to be constant, the electron temperature at the matching point must be calculated from the ionization/acceleration region.

3.2. Presheath region

The presheath is defined technically as the region where an electric field is required to accelerate the ions to the Bohm velocity at the Tonks–Langmuir edge before entering the sheath [28]. Based on the assumptions made in this work for this region, a similar work was previously done with an assumption of constant ionization frequency throughout the presheath domain [33]. This study also assumes the constant ionization frequency in the presheath region. The average ionization frequency in the presheath region is taken as the required constant. This assumption is justified as a reasonable one by the following: the ionization frequency is given by $\nu_\mathrm{i} = n_\mathrm{n}\langle\sigma_\mathrm{i}v_\mathrm{e}\rangle = n_\mathrm{n}RR_\mathrm{i}(T_\mathrm{e})$, where ν_i is the ionization frequency, n_n is the neutral number density and $\langle\sigma_\mathrm{i}v_\mathrm{e}\rangle = RR_\mathrm{i}(T_\mathrm{e})$ is the ionization reaction rate which can only be a function of electron temperature. Since a constant electron temperature in the presheath region is already assumed and the neutral number density is almost constant in the region near the anode, it is expected that the ionization frequency does not have much variation in the presheath region. To be more accurate, the neutral number density may be obtained from presheath solutions such as ion mean velocity and plasma number density using neutral and ion continuity equations.

The governing equations based on the aforementioned assumptions are as follows:

$$\frac{\mathrm{d}\Gamma_\mathrm{n}}{\mathrm{d}z} = -S, \qquad \frac{\mathrm{d}\Gamma_\mathrm{i}}{\mathrm{d}z} = S, \qquad \frac{\mathrm{d}\Gamma_\mathrm{e}}{\mathrm{d}z} = S \tag{9}$$

$$\frac{\mathrm{d}(n_\mathrm{e}u_\mathrm{i}^2)}{\mathrm{d}z} = -\frac{en_\mathrm{e}}{m_\mathrm{i}}\frac{\mathrm{d}\varphi}{\mathrm{d}z} \tag{10}$$

$$0 = -kT_\mathrm{e}\frac{\mathrm{d}n_\mathrm{e}}{\mathrm{d}z} + en_\mathrm{e}\frac{\mathrm{d}\varphi}{\mathrm{d}z} \tag{11}$$

where the subscripts n, i and e represent neutral, ion and electron, respectively, $\Gamma = nu$ is the species number flux, and S is the ionization source term, which is given by $S = n_\mathrm{e}n_\mathrm{n}\langle\sigma_\mathrm{i}v_\mathrm{e}\rangle$. The regression equation for the ionization source term is generated by numerical integration of experimental data for the ionization cross section at a given electron temperature with Maxwellian velocity distribution for electrons. Only the first ionization is considered. The experimental cross section data for the xenon first ionization collision is taken from [34]. Other reaction rates are also obtained using the same method. In the presheath region, there are five unknowns: neutral number density, plasma number density, ion mean velocity, electron mean velocity, and electric potential. Equation (9) can provide

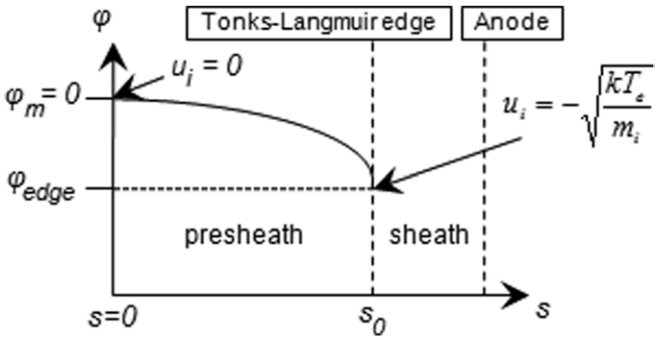

Figure 4. Non-dimensional coordinate and boundary conditions for the presheath region.

two useful relations, global continuity and current continuity given in (12) and (13), respectively:

$$m_\mathrm{n}n_\mathrm{n}u_\mathrm{n} + m_\mathrm{i}n_\mathrm{e}u_\mathrm{i} = \text{const.} = \frac{\dot{m}}{A} \tag{12}$$

$$n_\mathrm{e}u_\mathrm{i} - n_\mathrm{e}u_\mathrm{e} = \frac{I_\mathrm{d}}{eA} \tag{13}$$

where $\dot{m}$ is the propellant mass flow rate, A is the thruster channel area and I_d is the discharge current. It is important to note that the global and current continuity equations must hold throughout the whole domain, not just restricted to the presheath region.

The presheath region is solved by following Kino and Shaw's work with the non-dimensional coordinate and boundary conditions shown in figure 4 [33].

Additional procedures to Kino and Shaw's work include the calculation of average ionization collision frequency, $\nu_\mathrm{i,ave}$, and correct neutral number density using the global continuity equation again. Once this is done, the electron mean velocity can be easily calculated using the current continuity equation.

From the solution procedure, the presheath length is varied depending on the neutral number density and electron temperature at the matching point as shown in

$$L_\mathrm{presheath} = \left(\frac{2kT_\mathrm{e}}{m_\mathrm{i}}\right)^{1/2}\frac{s_0}{\nu_\mathrm{i,ave}}. \tag{14}$$

The dependence of the presheath length on neutral number density is weak. However, the electron temperature at the matching point has significant effects on the presheath length. If the electron temperature at the matching point increases, the average ionization collision frequency also increases. Although the term $(2kT_\mathrm{e}/m_\mathrm{i})^{1/2}$ also increases, the effect of increasing the average ionization collision frequency is dominant and this results in a decrease in the presheath length.

Note that by the sheath and presheath solution, the value of electric potential at the matching point as well as the presheath length can be determined. Furthermore, the value of plasma number density at the Tonks–Langmuir edge can also be determined which gives a self-consistent method. In addition, because this solution method is entirely analytical, the method is highly efficient.

3.3. Ionization/acceleration region

In this region, six unknowns must be determined, which are the same unknowns as those in the presheath region and electron temperature. The governing equations are as follows:

$$u_n \frac{dn_n}{dz} = -S, \qquad \frac{d\Gamma_i}{dz} = S, \qquad \frac{d\Gamma_e}{dz} = S \tag{15}$$

$$n_e(z) = \int_0^z \frac{S(z')\,dz'}{[u_{n,0}^2 + 2(e/m_i)(\varphi(z') - \varphi(z))]^{1/2}} + \frac{n_{e,0}u_{i,0}}{[u_{n,0}^2 + 2(e/m_i)(\varphi_0 - \varphi(z))]^{1/2}} \tag{16}$$

$$\frac{d(e\varphi)}{dz} = \frac{m_e \nu_{e,m}}{n_e}\Gamma_e \tag{17}$$

$$\frac{d\varepsilon_e}{dz} = -\frac{3}{5}eE - \frac{3}{5}\frac{n_e \nu_{e,\varepsilon}}{\Gamma_e}\varepsilon_e - \frac{n_e \nu_i}{\Gamma_e}\varepsilon_e. \tag{18}$$

Continuity equations are all the same as those for the presheath region as well as the global and current continuities. The integration is performed only for the neutral continuity equation. The boundary condition is the neutral number density at the matching point. Since the ion mean velocity is 0 there, the neutral number density at the matching point is directly calculated from the propellant mass flow rate. Consequently, the neutral number density in the presheath region is higher than that from the given propellant mass flow rate. This accounts for the ion recombination back to neutral at the anode due to ion backflow.

In (16), the lower integration limit, 0, represents the matching point and thus $u_{n,0}$ and $u_{i,0}$ are the neutral and ion mean velocity at the matching point. The ion momentum equation is not used to prevent negative plasma number density from occurring during integration and enhance numerical robustness. Equation (16), called the ion flux-tube equation, cannot be used for the following case:

$$\begin{aligned} 2\frac{e}{m_i}(\varphi(z') - \varphi(z)) &\leqslant -u_{n,0}^2 \\ 2\frac{e}{m_i}(\varphi_0 - \varphi(z)) &\leqslant -u_{n,0}^2. \end{aligned} \tag{19}$$

In order not to have the conditions in (19), the electric potential should keep decreasing from the matching point to the cathode. The second term in (16) accounts for the initial ion flux at the matching point [35]. Although the ion mean velocity is zero at the matching point, it should have the value of neutral velocity to have a solution of the plasma number density. It is a phenomenological result from numerical experimentations. If it were not included, the plasma number density right beside the matching point would have a significantly low value and show discontinuity. The reason why it should be included can also be explained from (2), where the ion mean velocity must be that of neutral at the matching point in order to have a regular singular point. Because the range of the ion mean velocity magnitude at the matching point is from 0 to at maximum the neutral mean velocity, which is relatively very small, the error from the different treatments on the ion mean velocity magnitude at the matching point is expected to be negligible. Equation (16) is an integral equation, so the integration is performed using the four-point Gauss–Legendre quadrature rule to obtain enough accuracy [36].

Boeuf's method is used to integrate equation (17) [6, 37]. The two boundary conditions, one at the matching point from the sheath/presheath solutions and the other at the cathode, which is assumed to be zero potential, allow the two dependent variables to be determined. The electron flux may be expressed using global and current continuity equations as

$$\Gamma_e(z) = \Gamma_e(c) - \Gamma_n(z) + \Gamma_n(c) \tag{20}$$

where c represents the cathode position. In this formulation, $\Gamma_e(c)$ becomes another unknown. $\nu_{e,m}$ is the classical cross field electron momentum collision frequency, with an effective electron momentum collision frequency and electron cyclotron frequency, and is given by

$$\nu_{e,m} = \nu_{e,eff}\left(1 + \frac{\omega_e^2}{\nu_{e,eff}^2}\right) \tag{21}$$

where ω_e is the electron cyclotron frequency and $\nu_{e,eff}$ is the effective collision frequency which includes the electron–neutral momentum collision, Coulomb collision, electron–wall collision and anomalous Bohm collision in the form of

$$\nu_{e,eff} = \nu_{en} + \nu_{ei} + \nu_{wall} + \alpha_{ano}\omega_e \tag{22}$$

where α_{ano} is the empirical coefficient to account for the anomalous Bohm collision frequency. The reaction rate for electron–ion Coulomb collision is calculated using the following formula [10]:

$$RR_{ei} = \langle \sigma_{ei} v_e \rangle = \frac{4\sqrt{2\pi}}{3}\left(\frac{m_e}{kT_e}\right)^{3/2}\left(\frac{e^2}{4\pi\varepsilon_0 m_e}\right)^2 \ln\Lambda \tag{23}$$

where $\ln\Lambda$ is called the Coulomb logarithm. The model of electron–wall collision is taken from [38]. The anomalous electron diffusion is still a debatable topic among HET researchers. Thus, the most recent experimental results are taken, which claim that the anomalous diffusion due to plasma turbulence has a dominant effect on the electron cross field diffusion compared with the electron–wall collision from the conclusion of the Fabry–Perot experiments for a 5 kW class HET [39]. The experimental results are compared with the hybrid numerical model to deduce the empirical coefficients for wall collision and Bohm-type diffusion. The same form of mobility expression for inside and outside of the channel and the values of each parameter given by

$$\mu_{\perp,in} \propto \frac{K_{in}}{16B}, \quad K_{in} = 0.1, \qquad \mu_{\perp,out} \propto \frac{K_{out}}{16B}, \quad K_{out} = 0.2 \tag{24}$$

where $\mu_{\perp,in}$ and $\mu_{\perp,out}$ are the electron cross field mobility inside and outside the channel, respectively. Ks are the empirical coefficients here. In order to adapt (24) to the current form of $\nu_B = \alpha_{ano}\omega_e$, the following curve fit equations are proposed to cover large discharge voltage variations. By letting

$\hat{\alpha}_{\text{ano}} = 1/\alpha_{\text{ano}}$,

(1) Inside the thruster channel:

$\hat{\alpha}_{\text{ano, min}} = 100$ at 150 V

$\hat{\alpha}_{\text{ano,max}} = 160$ over 400 V

$$\hat{\alpha}_{\text{ano}} = \hat{\alpha}_{\text{ano,min}} \left[1 - \exp\left\{ A \left(\frac{V_{\text{d}} - 400}{400 - 150} \right)^2 \right\} \right] + \hat{\alpha}_{\text{ano,max}} \tag{25}$$

where

$$A = \log\left(1 + \frac{\hat{\alpha}_{\text{ano,max}} - \hat{\alpha}_{\text{ano,min}}}{\hat{\alpha}_{\text{ano,min}}} \right).$$

(2) Outside the thruster channel:

$$\hat{\alpha}_{\text{ano,min}} = 50 \qquad \text{at } 150\text{ V}$$

$$\hat{\alpha}_{\text{ano,max}} = 80 \qquad \text{over } 400\text{ V}.$$

The same form is used as that inside the channel.

Furthermore, in order to have numerical stability, the smooth variation of $\hat{\alpha}_{\text{ano}}$ is implemented as

$$\hat{\alpha}_{\text{ano}}(z) = \begin{cases} \hat{\alpha}_{\text{ano,in}} & z \leqslant L \\ \dfrac{\hat{\alpha}_{\text{ano,in}} - \hat{\alpha}_{\text{ano,out}}}{2} \cos\left(\dfrac{z - L}{L_{\text{s}}} \pi \right) + \dfrac{\hat{\alpha}_{\text{ano,in}} + \hat{\alpha}_{\text{ano,out}}}{2} & L \leqslant z \leqslant L + L_{\text{s}} \\ \hat{\alpha}_{\text{ano,out}} & z \geqslant L + L_{\text{s}} \end{cases} \tag{26}$$

where L is the thruster channel length and L_{s} is the smooth transition distance. Here, L_{s} is taken to be half of the distance from the thruster exit to the cathode line.

In (18), $\varepsilon_{\text{e}} = 3/2kT_{\text{e}}$ is the electron internal energy and $\nu_{\text{e},\varepsilon}$ is the electron energy loss frequency which consists of several loss mechanisms such as ionization, excitation and wall-collision energy losses. The electron temperature at the cathode is usually taken to be 2–3 eV. Here, 2 eV is taken as a boundary condition.

The energy loss rate by ionization and excitation is given by

$$\varepsilon_{\text{e}} \nu_{\text{ion/exc}} = \varepsilon_{\text{ion}} \nu_{\text{i}} + \varepsilon_{\text{exc}} \nu_{\text{exc}} \tag{27}$$

where ε_{ion} is the threshold energy of first ionization for xenon, 12.129 84 eV, ε_{exc} is the threshold energy of first excitation level for xenon, 8.32 eV, ν_{i} is the ionization frequency and ν_{exc} is the excitation collision frequency. For the wall-collision energy loss frequency, the model suggested in [38] is implemented.

The neutral continuity, electron momentum, and electron energy equations are solved with the finite difference method.

3.4. Matching two solutions

In order to match two solutions, all the values of the unknowns from each region must be the same at the matching point. Since the unknowns are neutral number density, ion mean velocity, electron mean velocity, electron temperature, plasma number density, and electric potential, proper strategies must be provided for each unknown. The strategies are as follows:

(1) Neutral number density: it is constant and fixed as the one obtained from the given propellant mass flow rate. This is a consequence of global continuity since the ion mean velocity is zero at the matching point. This value also plays the role of boundary condition for neutral number density integration in the ionization/acceleration region. The neutral number density distribution in the presheath is obtained from global continuity.

(2) Ion mean velocity: it is zero at the matching point. This is a consequence from the assumption of dividing the whole domain into two regions since the presheath region starts from the edge of the main plasma body where the ion mean velocity is equal to zero. This value also plays the role of one of the boundary conditions in the presheath region. Ion mean velocity distribution in the ionization/acceleration region is obtained from global continuity.

(3) Electron mean velocity: it is obtained from the solution of the ionization/acceleration region by solving the electron momentum equation. From those solutions, the electron flux at the cathode is obtained and the electron mean velocity is then calculated using current continuity for the whole domain once the plasma number density and ion mean velocity for the whole domain are known. Another fact is that the current at the matching point comes from thorough electron flux and is equal to the discharge current.

(4) Electron temperature: it is calculated by solving the electron energy equation in the ionization/acceleration region with a boundary condition of electron temperature at the cathode. The electron temperature in the presheath region is assumed to be constant as the value of the matching point.

(5) Plasma number density: it is assumed first. After obtaining solutions from the ionization/acceleration region, the electron temperature at the matching point and discharge current are known. In order to update plasma number density at the matching point, the current continuity is employed. The total current at the Tonks–Langmuir edge is calculated, which allows the plasma number density to be updated using the relation

$$\frac{I_{\text{d}}}{eA} = (n_{\text{e}} u_{\text{i}} - n_{\text{e}} u_{\text{e}})|_{\text{edge}} = n_{\text{e,m}} \exp\left[-\frac{e\varphi_{\text{m-edge}}}{kT_{\text{e}}} \right] \left[-\sqrt{\frac{kT_{\text{e}}}{m_{\text{i}}}} + \sqrt{\frac{kT_{\text{e}}}{2\pi m_{\text{e}}}} \right]. \tag{28}$$

Plasma number density distribution in the presheath is obtained using the Boltzmann relation.

(6) Electric potential: it is obtained from the sheath/presheath solution, which also plays the role of a boundary condition for electron momentum equation in the ionization/acceleration region.

By iteratively applying the strategies above to match two solutions, the final converged solution can be obtained. The under-relaxation scheme is implemented to ensure numerical

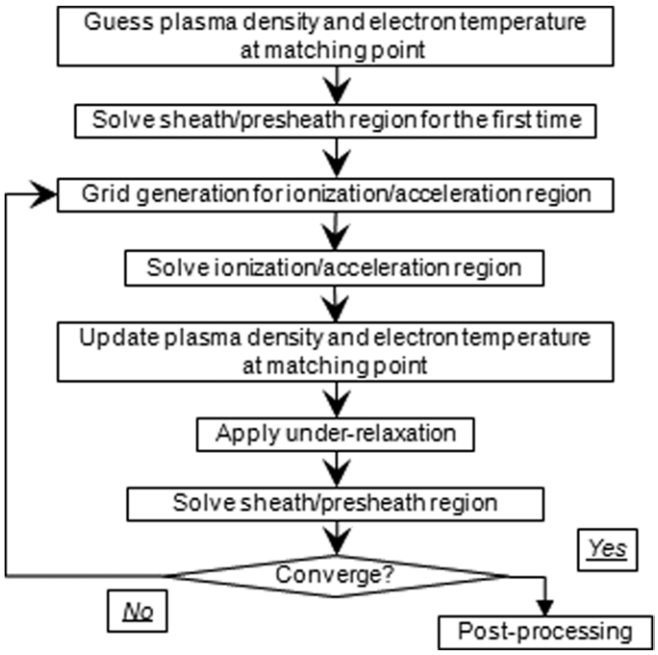

Figure 5. Diagram of solution procedure.

robustness, which is given by

$$V^k = \alpha_{\text{relax}} V^k + (1 - \alpha_{\text{relax}}) V^{k-1} \tag{29}$$

where k is the iteration step, V is the dependent variable vector and α_{relax} is the relaxation coefficient, and for under-relaxation, it has a value between 0 and 1.

A diagram of the solution procedure is shown in figure 5. In conclusion, the proposed method presented in this section possesses self-consistency from the fact that all the dependent variables are determined by the method. The solution procedure is numerically robust by avoiding singular formulation. Furthermore, the method does not depend on the initial guesses.

4. Results and discussion

4.1. Validations on performance parameters

In order to validate the developed method, the experimental results are taken for the SPT-100 thruster [40]. The authors of [40] use a 1D hybrid method and compare their results with experimental data. Because there has been no published literature which validates the results from their 1D macroscopic fluid models with experimental data of actual thrusters, the results of the developed method are also compared with the computational results of [40]. The geometry and input parameters of the SPT-100 are shown in table 1.

The magnetic field distribution inside the channel of the SPT-100 is given in the analytical form as

$$B(z) = B_{\max} \exp\left[-K\left(\frac{z}{L} - 1\right)^2\right] \tag{30}$$

where K is the magnetic field shape coefficient. For the SPT-100, K has a value of 16. The maximum magnetic field is located at the thruster channel exit line, and for the region outside the channel, where significant magnetic field still exists, linear distribution is assumed as in [40].

Table 1. Geometry and input parameters of the SPT-100.

Geometry	Value	Parameter	Value
Outer radius	5.0 cm	$B_{\max}$	160 G
Inner radius	3.5 cm	B_{cathode}	130 G
Channel length	4.0 cm	Mass flow rate (Xe)	4.9 mg s^{-1}
Length from exit to cathode	2.0 cm	Discharge voltage	300 V

Table 2. Comparisons between simulation results and experimental data.

Parameter	Experiment	Hybrid 1D method [40]	Self-consistent method
I_{sp} (s)	1600	1500 (−6%)	1728 (+8%)
Thrust (mN)	83	90.2 (+9%)	82 (−1%)
Efficiency (%)	50	60 (+20%)	49 (−2%)
I_{d} (A)	4.5	3.7 (−18%)	4.76 (+6%)
Calculation time of the self-consistent method ∼ 22 s.			

The specific impulse is calculated as

$$I_{\text{sp}} = \frac{u_{\text{i,c}}}{g_0} \tag{31}$$

where $u_{\text{i,c}}$ is the ion mean velocity at the cathode line, and g_0 is the gravitational acceleration at the Earth's surface. The thrust is obtained from

$$T = \dot{m}_{\text{i,c}} u_{\text{i,c}} \tag{32}$$

where $\dot{m}_{\text{i,c}}$ is the ion mass flow rate at the cathode line. The discharge current is obtained from

$$I_{\text{d}} = e n_{\text{e}} u_{\text{e}}|_{\text{m}} A \tag{33}$$

where $n_{\text{e}} u_{\text{e}}|_{\text{m}}$ is the electron flux at the matching point, and A is the thruster channel area. The discharge current is directly calculated at the matching point since the ion velocity is zero at this location. Finally, the efficiency is obtained as

$$\eta = \frac{T^2}{2\dot{m} P_{\text{d}}} \tag{34}$$

where $\dot{m}$ is the given propellant mass flow rate, and P_{d} is the discharge power, which is calculated as $P_{\text{d}} = V_{\text{d}} I_{\text{d}}$. V_{d} is the discharge voltage. Although all the required input powers are not included in (34), the discharge power is taken as the input power based on the observation that most of the power is used for the discharge.

The comparisons of the calculated performance metrics with the experimental data and the results of [40] are shown in table 2.

In table 2, the percentage values in parentheses are the differences from experimental data. All the differences of the developed method are less than 10% and it shows better accuracy than [40] and more consistent error distribution for the compared metrics. The calculated specific impulse shows the biggest difference (+8%). This may be caused by neglecting ion–wall recombination and plume expansion loss. The calculation time of 22 s proves the high numerical efficiency of the developed method.

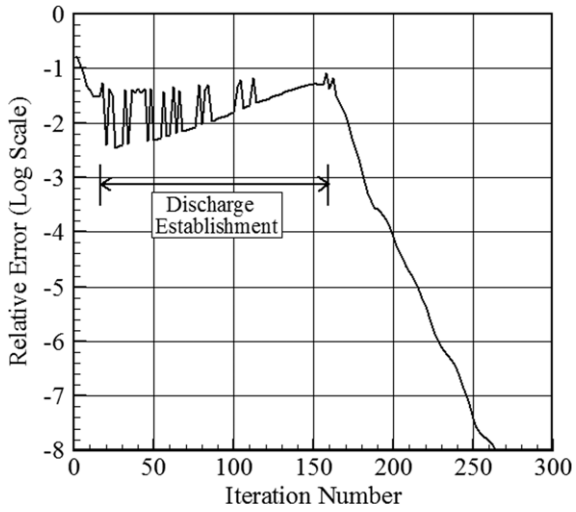

Figure 6. Error convergence history.

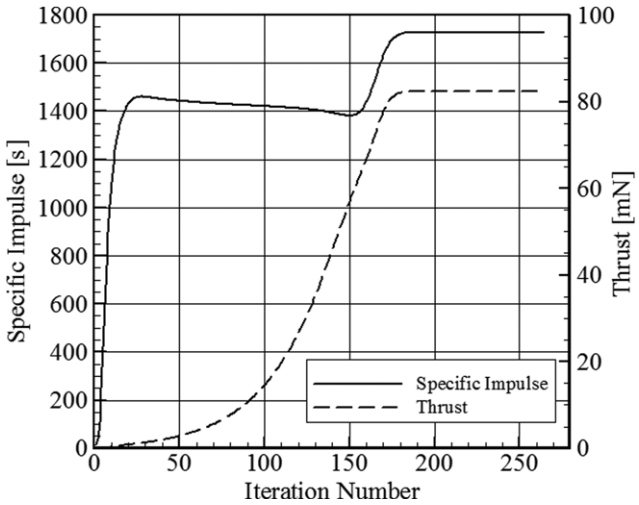

Figure 7. Convergence histories of I_{sp} and thrust.

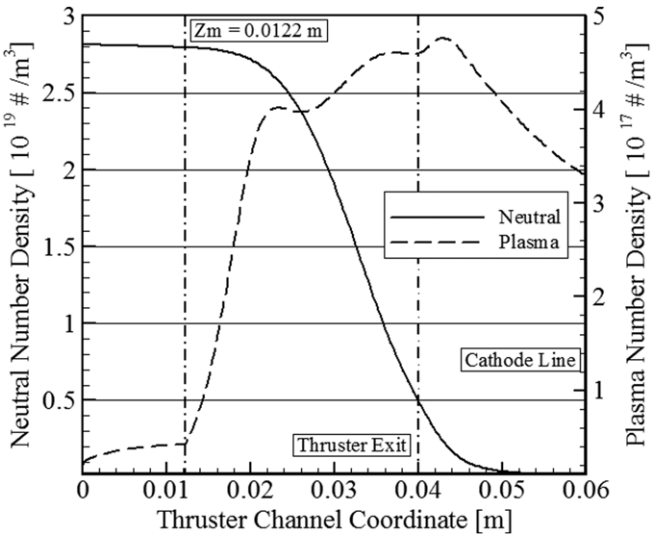

Figure 8. Neutral and plasma number density distributions.

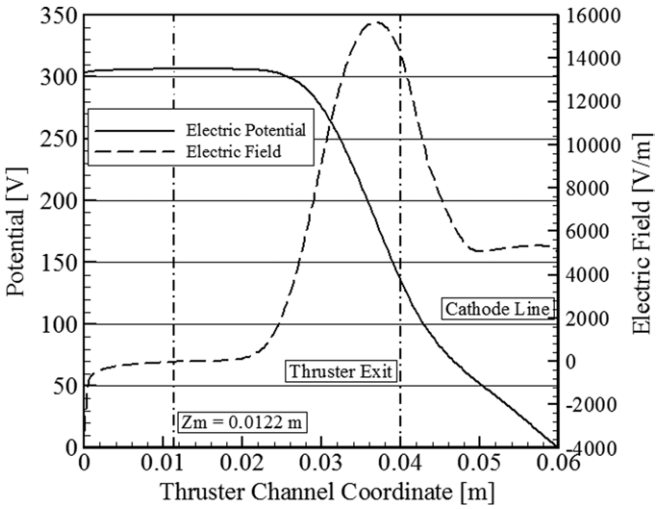

Figure 9. Electric potential and electric field distributions.

4.2. Convergence characteristics

The condition of convergence is checked with the relative changes in dependent variables between two consecutive iteration steps. The error convergence history is shown in figure 6.

The initial half part of the history shows oscillation and a slight growth. Since the initial guesses of electron temperature and plasma number density distributions are quite low, it can be thought that the discharge is established during that part of the history by resembling time-accurate startup transient phenomena. Once the pseudo-discharge process is established, the convergence rate becomes very high.

Figure 7 shows the convergence histories of specific impulse and thrust. After about 180 iterations, these metrics reach almost constant values and stay at those values until convergence is achieved.

4.3. Plasma structures

Figure 8 shows the neutral number density and plasma number density distributions. Many of the neutrals are exhausted near the thruster exit plane, which gives only 17.6% of the anode neutral number density at the exit. The lower values of neutral number density are observed outside the channel. Plasma number density variation in the presheath is small and after the matching point, the increase in plasma number density is quite significant. The peak value of plasma number density is found slightly outside the channel from the thruster exit, and then it decreases toward the cathode line.

Figure 9 shows the electric potential and electric field distributions. The electric potential from the anode sheath edge to a certain front part of the ionization/acceleration region exhibits almost plane and constant values. However, the correct shape is convex with the center of the cone at the matching point; then it keeps decreasing until the cathode line. The electric potential at the thruster exit plane is about 130 V and it drops downstream outside the thruster toward the cathode.

The electric field distribution shows that the electric field in the presheath region is negative, which causes the ions to flow toward the anode and the peak value of the electric field

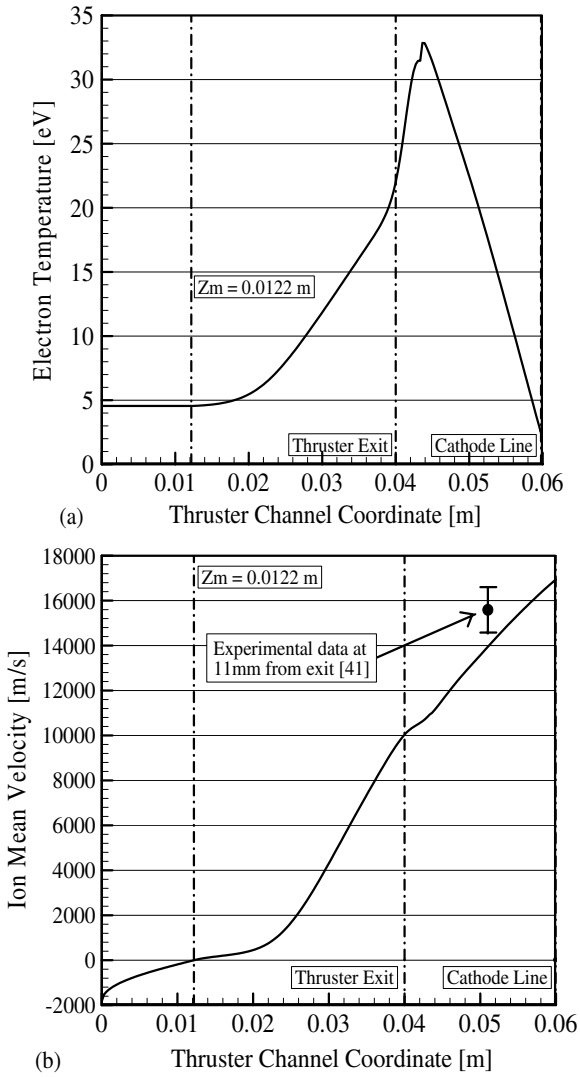

Figure 10. (*a*) Electron temperature and (*b*) ion mean velocity distributions.

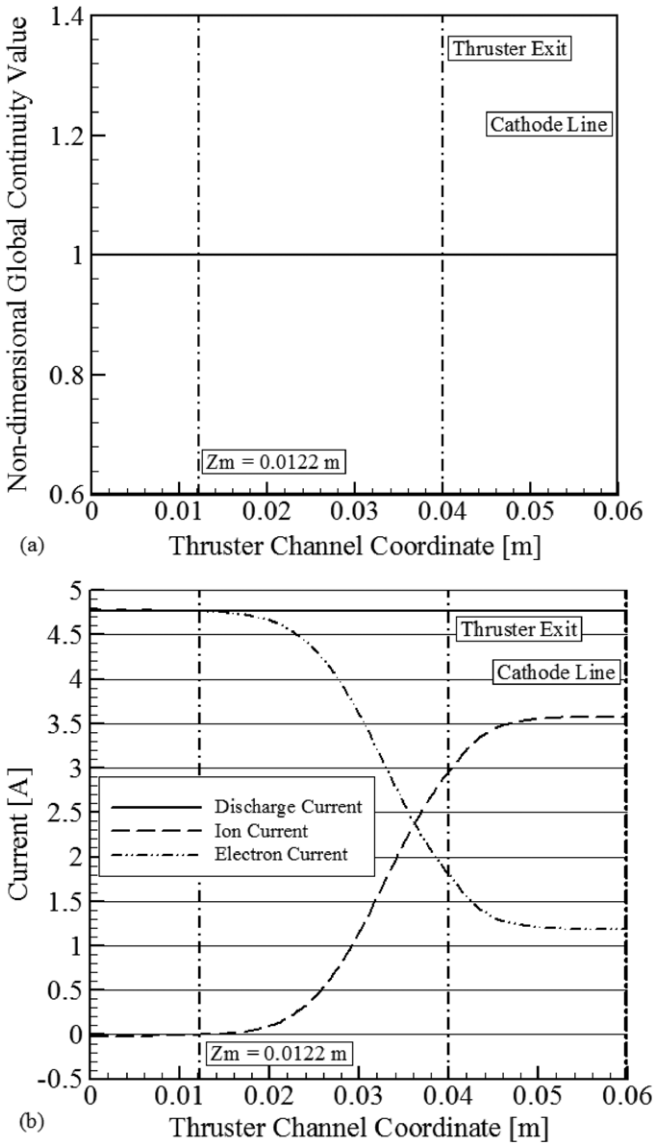

Figure 11. (*a*) Global continuity in non-dimensional value and (*b*) current continuity in dimensional value.

is located 3.3 mm inside the thruster channel from the exit plane.

Figure 10 shows the electron temperature and ion mean velocity distributions. The electron temperature in the presheath region has a constant value and it extends slightly to the ionization/acceleration region. It has a peak value of about 33 eV slightly outside the channel from the exit line. Ion mean velocity distribution shows the negative mean velocity in the presheath region. In the ionization/acceleration region, it keeps increasing by the electric field. The dot and error bar in the ion mean velocity plot indicates an experimental ion mean axial velocity measured 11 mm away from the thruster exit, which is taken from [41]. Closer agreement with the calculated one is identified.

Figure 11 shows that the global and current continuities are well satisfied for the whole domain. Furthermore, figure 11(*a*) shows the non-dimensional value of the right-hand side term in the global continuity equation, which is 1. Figure 11(*b*) also shows the ion and electron current contributions throughout the domain. As expected, almost all the current near the anode is carried by electrons. At the cathode line, the electron current is greater than 1 A, which decreases the total efficiency. In order to have higher efficiency and higher specific impulse, it is important to increase the electrical efficiency, i.e. the ratio of ion current to discharge current, which is 0.75 in this case.

Figure 12 shows the ionization rate and electron Hall parameter distributions. As expected, the ionization rate has a peak value near the maximum magnetic field location. However, since the neutral number density also contributes to the ionization rate, the position of the peak ionization rate occurs upstream the location of the maximum magnetic field, where the neutral number density is quite low. The electron Hall parameter has values on the order of 100, which agrees with experimental data.

4.4. Limitations of the developed method

Since the solutions from each region with different assumptions are matched at the common face, some plasma variables such as plasma number density and electron mean

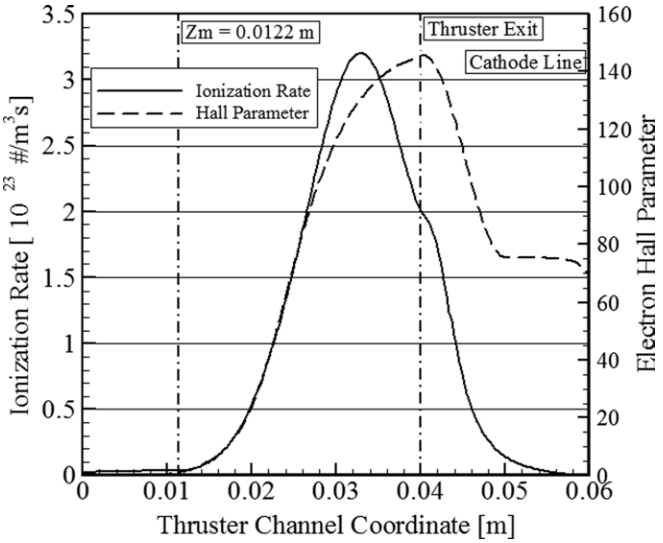

Figure 12. Ionization rate and electron Hall parameter distributions.

velocity show non-physical behavior around the matching point.

In figure 13, the first derivatives of the plasma number density and electron mean velocity profiles are discontinuous at the matching point, which is enclosed by a dotted circle. The division of the solution is necessary to ensure that the method is numerically robust and self-consistent, and thus the sacrifice in accuracy of certain plasma variables around the matching point is acceptable. Furthermore, the overall behaviors of plasma number density and electron mean velocity are quite reasonable compared with previous work and experimental data and it does not violate any of the continuity equations as seen in figure 11.

Another limitation of the developed method is on solvable magnetic field distributions. The magnetic field distribution is given in the analytical form as equation (38). If K decreases, the magnetic field strength at the anode tends to increase, as shown in figure 14. For sufficiently small K, it is identified that the developed method does not have a converged solution. As K decreases, the electron temperature at the matching point calculated by solving the electron energy equation in the ionization/acceleration region tends to increase, which results in a significant decrease in the presheath region length. The decrease in the presheath region length with electron temperature at the plasma body is correct physics since the higher collision phenomena shorten the collisionless presheath region. Since the presheath region collapses in a very thin region near the anode, it cannot be solved on a macroscopic scale of the current method. However, this should not be a problem since a large magnitude of the magnetic field strength is not required near the anode.

4.5. Remarks on anomalous diffusion coefficients

The anomalous coefficient calculations given in (25) and (26) are only a function of discharge voltage and over 400 V those are fixed as $\hat{\alpha}_{\text{ano,in}} = 160$ and $\hat{\alpha}_{\text{ano,out}} = 80$. Furthermore, the reference from which (25) and (26) are derived obtained the results only from the comparison of a 5 kW HET. In order to verify these simple relations for the anomalous coefficients,

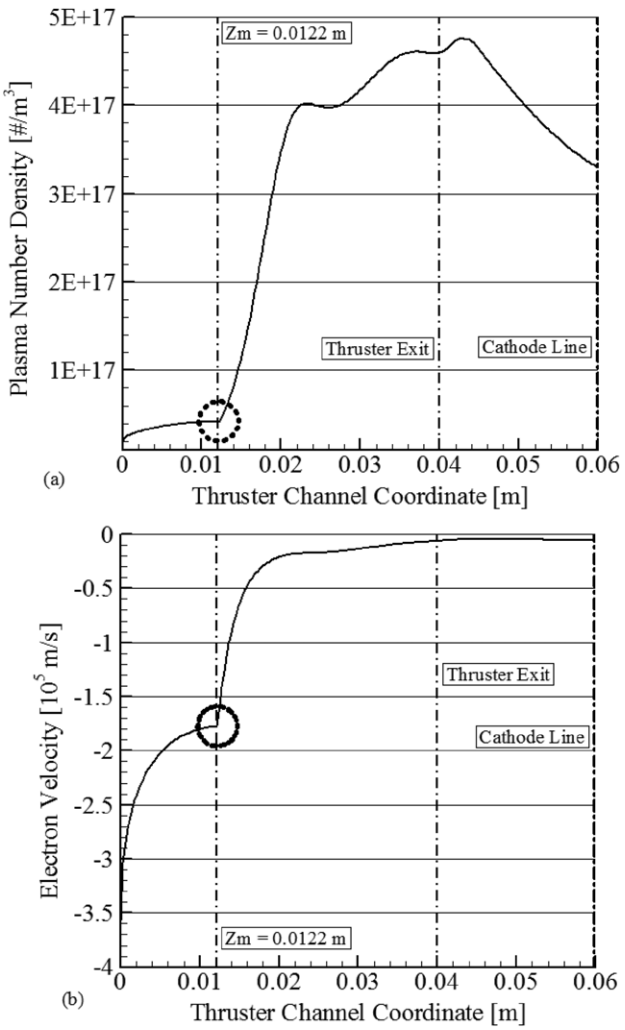

Figure 13. (*a*) Plasma number density distribution and (*b*) electron mean velocity distribution.

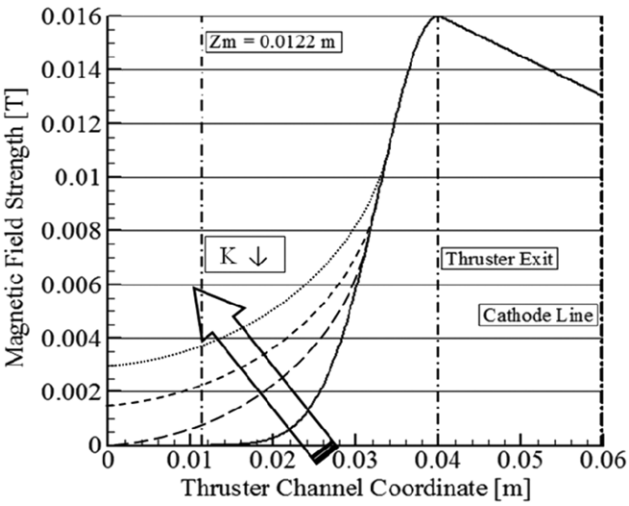

Figure 14. Variation of magnetic field distribution with K.

further validation is conducted with the variation of the anode propellant mass flow rate. The experimental data are taken from table V of [42]. The specific impulse and efficiency in the experimental data include the cathode mass flow rate.

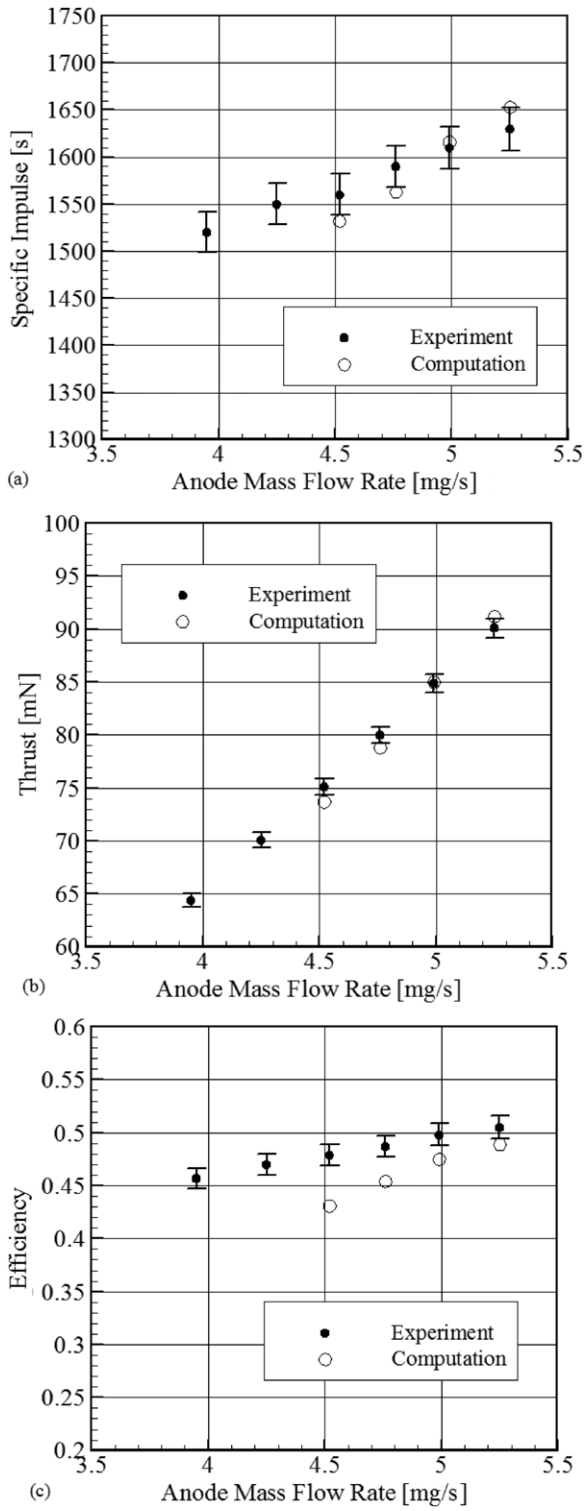

Figure 15. Validation results of the SPT-100 with the anode mass flow rate variation: (*a*) specific impulse (*b*) thrust and (*c*) efficiency.

The discharge voltage is 301 V, which corresponds to the anomalous coefficients based on (25) and (26) of

$$\hat{\alpha}_{\mathrm{ano,in}} = 152 \qquad \text{and} \qquad \hat{\alpha}_{\mathrm{ano,out}} = 76.$$

Figure 15 shows the simulation results and the experimental data. All computations are obtained with the same initial guesses. The error bar for the experimental results in figure 15 is based on [42]. The accuracy of the thrust stand and the flow rate has both ±1% error ranges. The error range of the discharge current is ±1.1% at a discharge current of 4.5 A. Based on these error ranges, the error of the specific impulse and the efficiency are estimated as ±1.4% and ±2.1%, respectively.

Figure 15 shows that the anomalous coefficients based on (25) and (26) give good accuracy for the specific impulse and the thrust near the design operation point of the SPT-100. However, the efficiency is estimated at a slightly lower value. Furthermore, for the mass flow rates lower and higher than the design operation point, the results deviate from experimental data. Even worse, use of fixed anomalous coefficients could not produce the solutions for the mass flow rates of 3.95 and 4.25 mg s^{-1}. This reveals that the anomalous coefficients should also be a function of other parameters such as the anode mass flow rate.

The anomalous diffusion cannot be solved with the current 1D macroscopic models, which require tuning of the anomalous coefficients to match experimental data. However, the anomalous coefficients can be treated as free parameters and then it is expected that the correct anomalous coefficients could be obtained to provide better accuracy in performance parameters compared with experimental data.

5. Validation with correct anomalous coefficients

The proposed formula for the anomalous coefficients in the previous sections shows some deficiency in prediction when compared with experimental data at off-design operating points of the SPT-100. Thus, the formula does not guarantee reliable estimation of the anomalous coefficients. One way of dealing with uncertainties of the anomalous coefficients is to treat them as free parameters and investigate their effects on the results. In this section, a design of experiment (DOE) is performed to find the correct anomalous coefficients, which best matches with the experimental data. To this end, the performance metrics are first redefined in more detail to include more parameters which characterize the HET performance.

5.1. Redefinition of performance metrics

The definition of thrust now includes the neutral contribution and it is defined as

$$T = \dot{m}_{\mathrm{i,c}} u_{\mathrm{i,c}} + \dot{m}_{\mathrm{n,c}} u_{\mathrm{n,c}} \tag{35}$$

where $\dot{m}_{\mathrm{n,c}}$ is the neutral mass flow rate at the cathode line, and $u_{\mathrm{n,c}}$ is the neutral mean velocity at the cathode line. The anode specific impulse is introduced as

$$I_{\mathrm{sp,ano}} = \frac{T}{\dot{m}_{\mathrm{a}} g_0} \tag{36}$$

where $\dot{m}_{\mathrm{a}}$ is the anode mass flow rate. The anode efficiency is also introduced as

$$\eta_{\mathrm{ano}} = \frac{T^2}{2\dot{m}_{\mathrm{a}} P_{\mathrm{d}}} \tag{37}$$

where P_d is the discharge voltage. The total power required to sustain the discharge can be expressed as

$$P_{tot} = P_d + P_{cath} + P_{mag} \tag{38}$$

where P_{cath} is the power required to operate the cathode, and it is usually significantly less than the discharge power, although it varies with cathode type. P_{mag} is the power required to produce the magnetic field and it will be zero if permanent magnets are used. If the specific impulse and efficiency include the cathode mass flow rate, those are termed as the total specific impulse and total efficiency, respectively. For these total quantities as well as total power, additional inputs are required such as

(1) percentage of $\dot{m}_c$ based on $\dot{m}_a$ (%): this is termed as pmc;
(2) percentage of P_{cath} based on P_d (%): this is termed as ppc;
(3) percentage of P_{mag} based on P_d (%): this is termed as ppm,

where $\dot{m}_c$ is the cathode mass flow rate. Therefore, if those inputs are provided, the following total quantities can be calculated.

(1) Total specific impulse:

$$I_{sp,tot} = \frac{T}{\dot{m}_{tot} g_0} = \frac{T}{(\dot{m}_a + \dot{m}_c) g_0} = \frac{T}{(1 + 0.01\text{pmc})\dot{m}_a g_0} = \frac{I_{sp,ano}}{(1 + 0.01\text{pmc})}. \tag{39}$$

(2) Total efficiency:

$$\eta_{tot} = \frac{T^2}{2\dot{m}_{tot} P_{tot}} = \frac{T^2}{(1 + 0.01\text{pmc})(1 + 0.01\text{ppc} + 0.01\text{ppm}) 2\dot{m}_a P_d} = \frac{\eta_{ano}}{(1 + 0.01\text{pmc})(1 + 0.01\text{ppc} + 0.01\text{ppm})}. \tag{40}$$

(3) Total power:

$$P_{tot} = P_d + P_{cath} + P_{mag} = P_d + 0.01(\text{ppc} + \text{ppm}) P_d = (1 + 0.01\text{ppc} + 0.01\text{ppm}) P_d. \tag{41}$$

5.2. Validation results with optimum anomalous coefficients

The specified ranges of the anomalous coefficients are explored by numerical experimentation. Numerical exploration for the anomalous coefficient variation is the same as investigating the electron anomalous diffusion effects in the ionization/acceleration region. From the discussion on the proposed formula for the anomalous coefficients in the previous section, lower bound and upper bound of $\hat{\alpha}_{ano,in}$ are taken as 100 and 160, respectively. For $\hat{\alpha}_{ano,out}$, 50 and 80 are taken as the lower and upper bounds, respectively.

In order to conduct numerical experiments, a six-level full factorial design is used to create an experiment table, which results in a total of 36 runs. Each numerical exploration is performed for each anode mass flow rate of the SPT-100 experimental data.

The effects of the anomalous coefficients on performance parameters can be revealed through statistical regression.

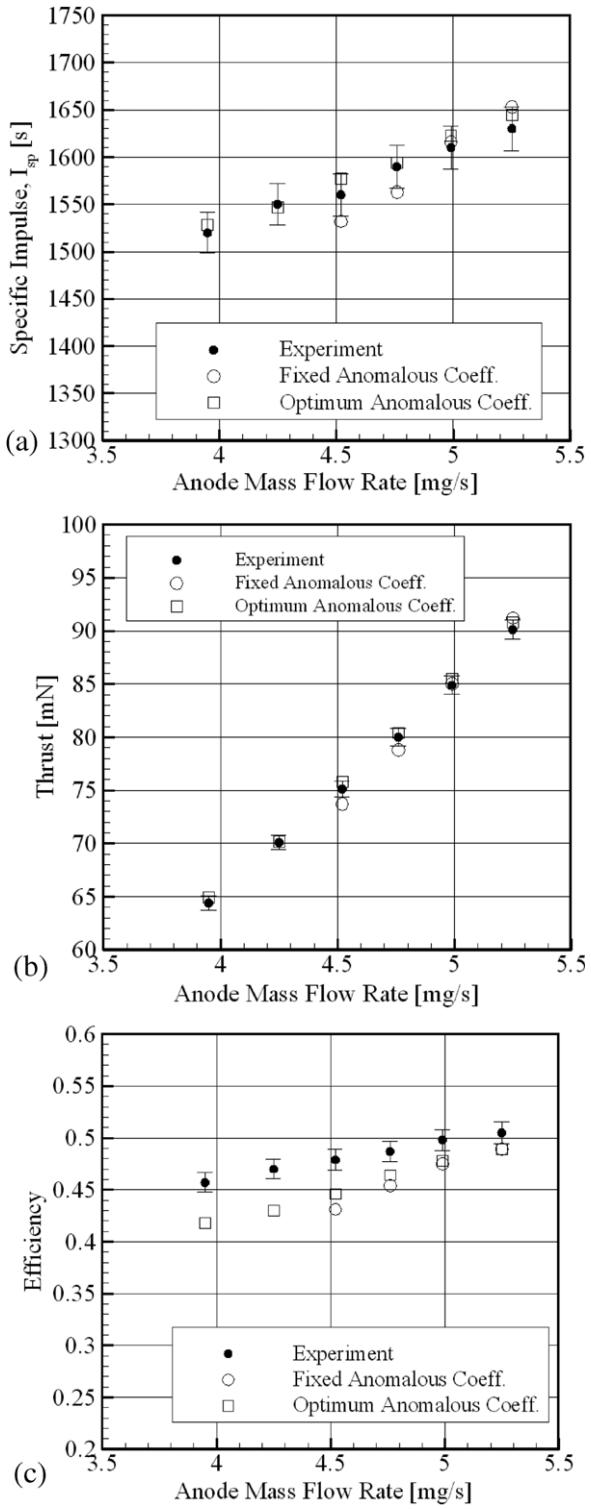

Figure 16. Comparison of experiments, fixed and optimum anomalous coefficients for the SPT-100: (*a*) total specific impulse, (*b*) thrust and (*c*) total efficiency.

Response surface equations from numerical experiments can be used to find the values of the correct anomalous coefficients closely matching the experimental data, where an optimization strategy is required. The optimization performance index should be differences between values from the response surface equations and experimental values, which can be expressed as

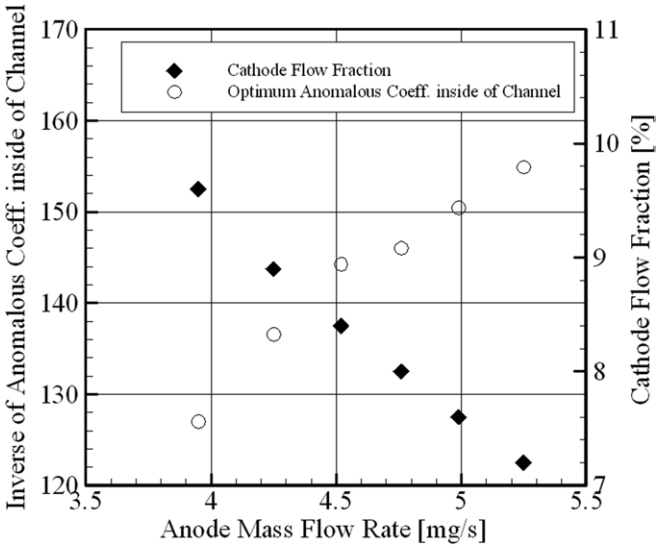

Figure 17. Variation of $\hat{\alpha}_{\mathrm{ano,in}}$ and cathode mass flow fraction with anode mass flow rate.

sum of square errors. Thrust, discharge current, total specific impulse and total efficiency are taken as the required responses to be matched for this purpose.

The optimization is conducted for all of the anode mass flow rate cases. Comparisons of total specific impulse, thrust, and total efficiency for fixed and optimum anomalous coefficients are shown in figure 16. Note that the developed method can produce solutions for the anode mass flow rates of 3.95 and 4.52 mg s^{-1}, which could not be obtained with the fixed values of the anomalous coefficients. This is due to the increase in axial electron diffusion. Using this optimization strategy yields very accurate predictions for the total specific impulse and thrust. However, prediction of the total efficiency still produces a slightly lower value than the experimental data for all cases. Nonetheless, it can be concluded that the use of optimum anomalous coefficients results in successful validation results for all validation points as well as for the cases of lower anode mass flow rates.

An interesting fact is that $\hat{\alpha}_{\mathrm{ano,in}}$ increases as the anode mass flow rate increases as shown in figure 17, while $\hat{\alpha}_{\mathrm{ano,out}}$ does not have a significant impact on performance parameters. The reason for this might be the effect of the cathode mass flow rate fraction, as also shown in figure 17. The cathode mass flow rate fraction increases as the anode mass flow rate is decreased. We infer that the anomalous coefficient inside the channel and the cathode mass flow rate fraction are positively correlated. This indicates that the increase in the cathode mass flow rate fraction causes a higher anomalous diffusion effect.

6. Conclusion

A self-consistent, robust and efficient methodology for 1D Hall thruster simulation is given. In order to achieve these characteristics simultaneously, novel approaches are taken based on the plasma physics characterizing the HET. Although the developed method shows discontinuities for the plasma number density and electron mean velocity profiles at the matching point, and it cannot solve for the case of high magnetic field distribution near the anode, the developed methodology can provide the capability of predicting correct performance parameters based on the validation results. The facts that there are no arbitrary conditions used for the SPT-100 and all computations are obtained by the same initial conditions indicate that the developed method can predict the performance of other thrusters at almost any operating condition as well as for different geometry variations. Use of these capabilities makes it possible that the correct anomalous coefficients closely matching the experimental data are found. Therefore it is expected that the developed method can be effectively used as a conceptual design tool for new HETs.

References

[1] Oh D Y 2005 *Proc. 41st AIAA/ASME/SAE/ASEE Joint Propulsion Conf. (Tucson, AZ)* (Washington, DC: American Institute of Aeronautics and Astronautics) AIAA-2005-4270
[2] Latocha V, Garrigues L, Degond P and Boeuf J P 2002 *Plasma Sources Sci. Technol.* **11** 104
[3] Adam J C, Heron A and Laval G 2004 *Phys. Plasmas* **11** 295
[4] Taccogna F, Longo S, Capitelli M and Schneider R 2005 *Phys. Plasmas* **12** 043502
[5] Taccogna F, Longo S, Capitelli M and Schneider R 2006 *Contrib. Plasma Phys.* **46** 781
[6] Boeuf J P, Garrigues L and Pitchford L C 1998 *Electron Kinetics and Application of Glow Discharge* ed U Kortshagen and L D Tsendin (New York: Plenum) p 85
[7] Ashkenazy J, Fruchtman A, Raitses Y and Fisch N J 1999 *Plasma Phys. Control. Fusion* **41** A357
[8] Fruchtman A, Fisch N J and Raitses Y 2000 *Proc. 36th AIAA/ASME/SAE/ASEE Joint Propulsion Conf. (Huntsville, AL)* (Washington, DC: American Institute of Aeronautics and Astronautics) AIAA 2000-3659
[9] Ahedo E, Gallardo J M and Martinez-Sanchez M 2002 *Phys. Plasmas* **9** 4061
[10] Roy S and Pandey B P 2002 *Phys. Plasmas* **9** 4052
[11] Cohen-Zur A, Fruchtman A, Ashkenazy J and Gany A 2002 *Phys. Plasmas* **9** 4363
[12] Dorf L and Semenov V 2003 *Appl. Phys. Lett.* **83** 2551
[13] Keidar M and Boyd I D 2001 *Phys. Plasmas* **8** 5315
[14] Serge B and Eduardo A 2009 *Phys. Rev.* E **79** 046401
[15] Fife J M 1998 *PhD Thesis* Massachusetts Institute of Technology
[16] Koo J W and Boyd I D 2003 *Proc. 39th AIAA/ASME/SAE/ASEE Joint Propulsion Conf. (Huntsville, AL)* (Washington, DC: American Institute of Aeronautics and Astronautics) AIAA-2003-4705
[17] Scharfe M K, Gascon N, Cappelli M A and Fernandez E 2006 *Phys. Plasmas* **13** 083505
[18] Hagelaar G, Bareilles J, Garrigues L and Boeuf J P 2002 *J. Appl. Phys.* **91** 5592
[19] Frank S G 1999 *PhD Thesis* The University of Michigan
[20] Dorf L A, Raitses Y F, Smirnov A N and Fisch N J 2004 *Proc. 40th AIAA/ASME/SAE/ASEE Joint Propulsion Conf. (Fort Lauderdale, FL)* (Washington, DC: American Institute of Aeronautics and Astronautics) AIAA-2004-3779
[21] Dorf L, Raitses Y, Fisch N J and Semenov V 2004 *Appl. Phys. Lett.* **84** 1070
[22] Dorf L, Raitses Y and Fisch N J 2005 *J. Appl. Phys.* **97** 103309
[23] Zhurin V V, Kaufman H R and Robinson R S 1999 *Plasma Sources Sci. Technol.* **8** R1–R20
[24] Bishaev A M and Kim V 1978 *Sov. Phys.—Tech. Phys.* **23** 1055
[25] Kim V 1998 *J. Propul. Power* **14** 736
[26] Ahedo E and Rus J 2005 *J. Appl. Phys.* **98** 043306

[27] Dorf L, Semenov V, Raitses Y and Fisch N J 2002 *Proc. 38th AIAA/ASME/SAE/ASEE Joint Propulsion Conf. (Indianapolis, IN)* (Washington, DC: American Institute of Aeronautics and Astronautics) AIAA-2002-4246
[28] Riemann K U 1991 *J. Phys. D: Appl. Phys.* **24** 493
[29] Ahedo E, Martinez P and Martinez-Sanchez M 2000 *Proc. 36th AIAA/ASME/SAE/ASEE Joint Propulsion Conf. (Huntsville, AL)* (Washington, DC: American Institute of Aeronautics and Astronautics) AIAA-2000-3655
[30] Ahedo E, Martinez P and Martinez-Sanchez M 2001 *Phys. Plasmas* **8** 3058
[31] Uribarri L and Choueiri E Y 2005 *Proc. 29th Int. Electric Propulsion Conf. (Princeton, NJ)* (Worthington, OH: The Electric Rocket Propulsion Society) IEPC-05-084
[32] Mitchner M and Kruger C H Jr 1973 *Partially Ionized Gases* (New York: Wiley) p 140
[33] Kino G S and Shaw E K 1966 *Phys. Fluids* **9** 587
[34] Szabo J J Jr 2001 *PhD Thesis* Massachusetts Institute of Technology
[35] Komurasaki K, Hirakawa M and Arakawa Y 1991 *Proc. 22nd Int. Electric Propulsion Conf. (Seattle, WA)* (Worthington, OH: The Electric Rocket Propulsion Society) IEPC-91-078
[36] Press W H, Teukolsky S A, Vetterling W T and Flannery B P 1992 *Numerical Recipes in FORTRAN* (New York: Cambridge University Press) p 745
[37] Boeuf J P and Garrigues L 1998 *J. Appl. Phys.* **84** 3541
[38] Ahedo E, Gallardo J M and Martinez-Sanchez M 2003 *Phys. Plasmas* **10** 3397
[39] Boniface C, Garrigues L, Hagelaar G J M, Boeuf J P, Gawron D and Mazouffre S 2006 *Appl. Phys. Lett.* **89** 161503
[40] Mikellides I G, Katz I, Mandell M J and Snyder J S 2001 *Proc. 7th AIAA/ASME/SAE/ASEE Joint Propulsion Conf. (Salt Lake City, UT)* (Washington, DC: American Institute of Aeronautics and Astronautics) AIAA-2001-3505
[41] David H M 1994 *Proc. 30th AIAA/ASME/SAE/ASEE Joint Propulsion Conf. (Indianapolis, IN)* (Washington, DC: American Institute of Aeronautics and Astronautics) AIAA-94-3141
[42] Sankovic J M, Hamley J A and Haag T W 1993 *Proc. 23rd Int. Electric Propulsion Conf. (Moscow, Russia)* (Worthington, OH: The Electric Rocket Propulsion Society) IEPC-93-094